

# Reversible Capture and Release of Cl<sub>2</sub> and Br<sub>2</sub> with a Redox-Active Metal–Organic Framework

Yuri Tulchinsky,<sup>†</sup> Christopher H. Hendon,<sup>†,‡</sup> Kirill A. Lomachenko,<sup>§,||</sup> Elisa Borfecchia,<sup>⊥</sup> Brent C. Melot,<sup>‡</sup> Matthew R. Hudson,<sup>#</sup> Jacob D. Tarver,<sup>#,∇</sup> Maciej D. Korzyński,<sup>†</sup> Amanda W. Stubbs,<sup>†</sup> Jacob J. Kagan,<sup>○</sup> Carlo Lamberti,<sup>⊥,||</sup> Craig M. Brown,<sup>#</sup> and Mircea Dincă<sup>\*,†,||</sup>

<sup>†</sup>Department of Chemistry, Massachusetts Institute of Technology, 77 Massachusetts Avenue, Cambridge, Massachusetts 02139, United States

<sup>‡</sup>Department of Chemistry, University of Southern California, 3620 McClintock Avenue, Los Angeles, California 90089-1062, United States

<sup>§</sup>European Synchrotron Radiation Facility, 71 Avenue des Martyrs, CS 40220, 38043 Grenoble Cedex 9, France

<sup>||</sup>IRC “Smart Materials”, Southern Federal University, Zorge Street 5, 344090 Rostov-on-Don, Russia

<sup>⊥</sup>Department of Chemistry, NIS, CrisDi, and INSTM Centre of Reference, University of Turin, Via Quarelo 15, I-10135 Torino, Italy

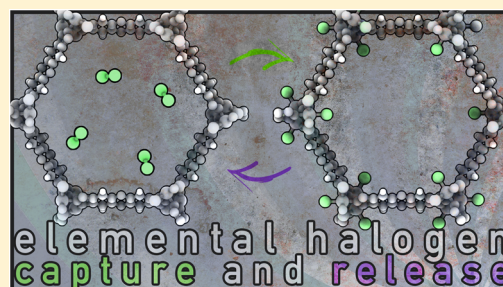
<sup>#</sup>Center for Neutron Research, National Institute of Standards and Technology, Gaithersburg, Maryland 20899, United States

<sup>∇</sup>National Renewable Energy Laboratory, 15013 Denver West Parkway, Golden, Colorado 80401, United States

<sup>○</sup>Department of Mathematics, Weizmann Institute of Science, 234 Herzl Street, Rehovot 7610001, Israel

## Supporting Information

**ABSTRACT:** Extreme toxicity, corrosiveness, and volatility pose serious challenges for the safe storage and transportation of elemental chlorine and bromine, which play critical roles in the chemical industry. Solid materials capable of forming stable nonvolatile compounds upon reaction with elemental halogens may partially mitigate these challenges by allowing safe halogen release on demand. Here we demonstrate that elemental halogens quantitatively oxidize coordinatively unsaturated Co(II) ions in a robust azolate metal–organic framework (MOF) to produce stable and safe-to-handle Co(III) materials featuring terminal Co(III)–halogen bonds. Thermal treatment of the oxidized MOF causes homolytic cleavage of the Co(III)–halogen bonds, reduction to Co(II), and concomitant release of elemental halogens. The reversible chemical storage and thermal release of elemental halogens occur with no significant losses of structural integrity, as the parent cobaltous MOF retains its crystallinity and porosity even after three oxidation/reduction cycles. These results highlight a material operating via redox mechanism that may find utility in the storage and capture of other noxious and corrosive gases.



## INTRODUCTION

Elemental halogens play key roles in a range of industrial processes. With an estimated annual production of 56 million tons, Cl<sub>2</sub> is widely used in water sanitation and is an essential ingredient in the production of plastics, such as poly(vinyl chloride) and polyurethanes, as well as solvents and pesticides.<sup>1</sup> Although used on a comparatively smaller scale, Br<sub>2</sub> is a key element in flame retardants, agricultural products, and pharmaceuticals.<sup>2</sup> The irreplaceable role of the elemental halogens in industry is contrasted with their extreme toxicity, corrosiveness, and volatility, which pose serious challenges for their safe handling, storage, and transportation. Despite decades of experience in mitigating these challenges, tragic accidents still occur worldwide as a result of leaks or explosions, making the development of new materials that can enable the open-air, safe-handling, and on-demand delivery of halogens highly

desirable. Metal–organic frameworks (MOFs), with their demonstrated utility in storing both inert and reactive gases, seem like logical choices for this challenge. However, despite thousands of reports on gas sorption and storage in MOFs, many including oxidizing or corrosive gases such as O<sub>2</sub>,<sup>3,4</sup> NO,<sup>5</sup> SO<sub>2</sub>,<sup>6,7</sup> and NH<sub>3</sub>,<sup>7–10</sup> to our knowledge none address the reversible storage of Br<sub>2</sub> or Cl<sub>2</sub>. The closest example is the irreversible bromination of an unsaturated organic ligand within a MOF and subsequent release of HBr upon treatment with base.<sup>11</sup> The lack of reports on reversible storage of the gaseous halogens (i.e., excluding I<sub>2</sub>) in MOFs is staggering given the interest in the field, but it highlights the difficulty in isolating

Received: March 7, 2017

Published: March 28, 2017

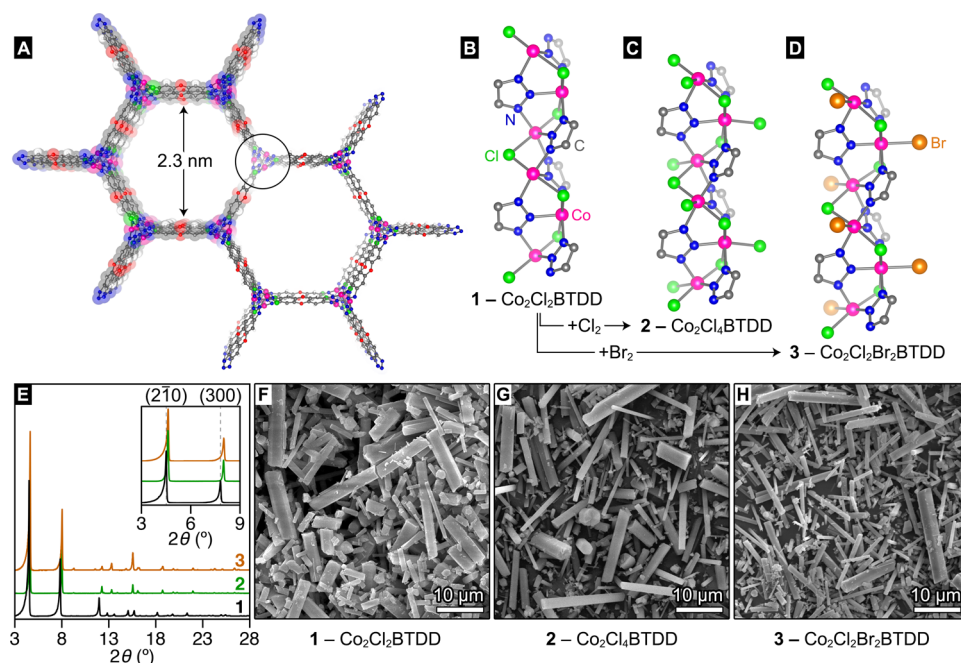


**Figure 1.** Structural and microscopy data. (A) A portion of the structure of the parent Co(II) MOF  $\text{Co}_2\text{Cl}_2\text{BTDD}$  (1) projected along the  $c$  axis. (B–D) SBU structures and local coordination environments of the Co centers in 1, 2, and 3, respectively, as determined by NPD. (E) PXRD data for 1, 2, and 3 showing retention of crystallinity and the lattice contraction in moving from 1 to 2 and 3, as evidenced by the upshift in the  $2\theta$  values for the (2-10) and (300) reflections. (F–H) Scanning electron micrographs of microcrystalline samples of 1, 2, and 3, respectively.

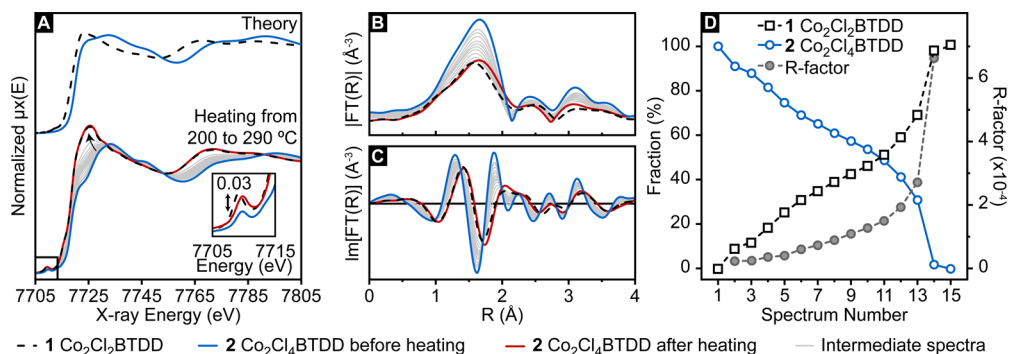


**Figure 2.** Co K-edge XAS characterization of 1 and 2. (A) (top) Theoretical XANES spectra for 1 and 2 calculated from the NPD structures. (bottom) Experimental XANES spectra at room temperature (RT) for 1, 2, 2 after heating, and intermediate states collected *in situ* in the 200–290  $^{\circ}\text{C}$  range during the thermal treatment of 2; the inset shows a magnification of the pre-edge peak at ca. 7709 eV. (B) Magnitudes and (C) imaginary parts of the phase-uncorrected Fourier transformed  $k^2$ -weighted EXAFS spectra,  $\text{FT}(R)$ . (D) Linear combination analysis of the whole series of *in situ* XANES spectra using the spectra of 1 and 2 at RT as references: relative fraction (open symbols) and fit quality factor (solid symbols).

materials that can reversibly bind halogens and release them over at least several cycles.

Although physisorption is the most widely employed mechanism for gas storage in porous materials, it is less effective with the lighter halogens because gas retention under ambient conditions is relatively poor and thus still requires the use of specialized storage and handling equipment. One historical shortcoming of MOFs for this application is their chemical instability toward  $\text{Cl}_2$  and  $\text{Br}_2$ . With reports of reversible redox cycling of MOFs,<sup>12,13</sup> we became intrigued by a chemical storage mechanism whereby  $\text{Cl}_2$  and  $\text{Br}_2$  could be stored by reduction to  $\text{Cl}^-$  and  $\text{Br}^-$  and subsequently released by oxidation back to their elemental  $\text{X}_2$  form. Here we report such a mechanism, where elemental  $\text{Br}_2$  and  $\text{Cl}_2$  reversibly oxidize Co(II) centers in  $\text{Co}_2\text{Cl}_2\text{BTDD}$  (1) (BTDD = bis(1*H*-1,2,3-triazolo[4,5-*b*],[4,5-*i*])dibenzo[1,4]dioxin) to form terminal cobalt(III) halides in  $\text{Co}_2\text{Cl}_2\text{X}_2\text{BTDD}$  ( $\text{X} = \text{Cl}$  (2),  $\text{Br}$  (3)).

To our knowledge, these are the first examples of all-Co(III) MOFs. We show that the Co(III) materials can be reduced back to Co(II) thermally, with concomitant liberation of  $\text{X}_2$ . These results represent the first example of reversible halogen uptake and release with a MOF and portend applications for halogen capture in the context of toxic gas removal and halogen storage in the context of safe handling of halogens.

## RESULTS AND DISCUSSION

**Robust Reactivity with Elemental Halogens and Formation of All-Co(III) MOFs.** Reaction of  $\text{H}_2\text{BTDD}$  with  $\text{CoCl}_2 \cdot 6\text{H}_2\text{O}$  results in the formation of solvated  $\text{Co}_2\text{Cl}_2\text{BTDD}$  (1), as previously described.<sup>10</sup> Rietveld analysis of neutron powder diffraction (NPD) data obtained from a sample of activated 1 at 10 K revealed a three-dimensional structure exhibiting one-dimensional channels arranged in a honeycomb fashion, similar to that reported for the Mn analogue

Mn<sub>2</sub>Cl<sub>2</sub>BTDD.<sup>10</sup> The secondary building units (SBUs) of **1** consist of infinite  $-(\text{Co}-\text{Cl})_n-$  chains coiled into threefold spirals and interconnected by the bis(triazolate) linkers (Figure 1A). Reaction of olive-green rodlike microcrystals of **1** with gaseous Cl<sub>2</sub> or PhICl<sub>2</sub> in dichloromethane results in rapid oxidation and quantitative formation of dark-brown microcrystals of Co<sub>2</sub>Cl<sub>4</sub>BTDD (**2**) (Figure 1B). A powder X-ray diffraction (PXRD) pattern of **2** revealed small but noticeable shifts in all of the reflection peaks toward higher scattering angles ( $2\theta$ ). These were most evident in the peaks corresponding to the (2 $\bar{1}$ 0) and (300) reflections (Figures 1C and S1), which shift from 4.5° and 7.8° in **1** to 4.6° and 8.0° in **2**, respectively. NPD analysis of **2** revealed decreases of 0.13 and 0.14 Å in the average Co–N and Co–Cl bond lengths, respectively, relative to those in **1**, as expected upon oxidation of Co(II) sites in **1** to Co(III) in **2**.

The stoichiometry of the oxidation of **1** to **2** in the presence of Cl<sub>2</sub> or PhICl<sub>2</sub> was ascertained by microelemental analysis (see the Supporting Information), X-ray absorption spectroscopy (XAS), and magnetometry. X-ray absorption near-edge spectroscopy (XANES) at the Co K-edges of **1** and **2** at room temperature revealed that the absorption edge of **2** is shifted by approximately 2 eV to higher energy relative to that of **1** (Figure 2A).<sup>14,15</sup> Although this shift cannot be used to quantify the degree of oxidation in **1**, it does indicate a higher average effective nuclear charge on the metal. This confirms that oxidation indeed takes place at the Co centers and not at the ligand, as had been previously observed, for instance, with the topologically related Mn<sub>2</sub>(2,5-dihydroxyterephthalate) (Mn-MOF-74) under similar oxidation conditions.<sup>16</sup> Magnetic measurements were particularly useful in determining whether the oxidation of Co(II) centers in **1** to Co(III) is quantitative because the latter are expected to exhibit low spin ( $S = 0$ ), whereas the former are paramagnetic. Temperature-dependent direct current (dc) susceptibility measurements on **1** between 2 and 300 K revealed typical Curie–Weiss behavior at 0.1 T. The susceptibility value at 300 K corresponds to a total effective magnetic moment of  $\mu_{\text{eff}} = 4.95\mu_{\text{B}}$  per Co, inferring high-spin ( $S = 3/2$ ) Co(II) centers (Figure S8). The magnetic behavior and effective moment of **1** are in line with those of the isostructural Co(II) system Co<sub>2</sub>(2,5-dihydroxyterephthalate)·(H<sub>2</sub>O)<sub>2</sub> (Co-MOF-74,  $\mu_{\text{eff}} = 4.67\mu_{\text{B}}$ ).<sup>17</sup> The oxidized compound **2** showed a diamagnetic response at all but the lowest temperatures, as expected for a low-spin d<sup>6</sup> complex in an octahedral crystal field. At 5 K, a small paramagnetic contribution was observed in the field-dependent low-temperature magnetization plots (Figure S9). We attribute this paramagnetic signal to magnetically dilute residual Co(II) centers. With the assumption that these exhibit an  $S = 3/2$  ground state, the saturation magnetization value of 0.15 $\mu_{\text{B}}$  at 5 K and 13 T corresponds to a Co(II) content of approximately 2.5% in **2**. Repeated experiments revealed that the residual Co(II) content in **2** is consistently low, varying between 1% and 6% depending on the batch and the number of consecutive treatments with oxidant. Thus, oxidation of **1** to **2** by Cl<sub>2</sub> or PhICl<sub>2</sub> is essentially quantitative, with isolated yields as high as 99%.

To further explore the scope of capture and release of other elemental halogens, we considered F<sub>2</sub>, Br<sub>2</sub>, and I<sub>2</sub>. Neither F<sub>2</sub> nor I<sub>2</sub> are feasible. Whereas Co(III) is not a sufficiently strong oxidizer to oxidize fluoride and release F<sub>2</sub> from Co(III)–F, **1** was found to be unreactive toward I<sub>2</sub>, suggesting that I<sub>2</sub> is too weak to oxidize Co(II) to Co(III)–I. On the other hand,

elemental Br<sub>2</sub> was found to possess redox behavior similar to that of Cl<sub>2</sub> and oxidized **1**. Prolonged exposure of **1** to Br<sub>2</sub> vapors results in quantitative conversion to Co<sub>2</sub>Cl<sub>2</sub>Br<sub>2</sub>BTDD (**3**), whose composition and bromine content were confirmed by microelemental analysis and inductively coupled plasma mass spectrometry (ICP-MS) after extensive vacuum treatment to remove unreacted, physisorbed Br<sub>2</sub> (Table S1). PXRD analysis of **3** revealed similar shifts of diffraction peaks as observed for **2**, with the most intense (2 $\bar{1}$ 0) and (300) reflections shifting to  $2\theta$  values indistinguishable from those seen for **2** (Figures 1C and S1). Oxidation of **1** and formation of Co(III)–Br was further confirmed by NPD analysis of **3**, which revealed only scattering for the framework skeleton and the terminal Co(III)-bound bromine atoms and no significant scattering from inside the pores. Similarly to **2**, **3** exhibits noticeably shorter average Co–N and Co–Cl bonds relative to **1**: 1.92 vs 2.12 Å and 2.34 vs 2.40 Å, respectively, as expected for moving from Co(II) to Co(III). Quantitative oxidation of **1** was confirmed by allowing free occupancy of the terminal bromide site in the Rietveld refinement process, which gave best fits when the occupancy was 100%. Importantly, the neutron diffraction experiments revealed no structural disorder between the terminal bromides and the bridging chlorides originating from **1**. Indeed, allowing the possibility of full or partial interchange of the bridging and terminal halide positions did not improve the fit parameters and in fact made them worse.

Oxidation of **1** by elemental halogens without bulk decomposition or microscopic framework collapse was also evidenced by scanning electron microscopy (SEM) and porosity measurements. Figure 1F–H shows that microcrystals of **1** maintain their hexagonal rodlike shape upon oxidation. N<sub>2</sub> adsorption isotherms on **2** and **3** revealed saturation uptakes of 585 cm<sup>3</sup>/g (306 463 cm<sup>3</sup>/mol) and 429 cm<sup>3</sup>/g (262 874 cm<sup>3</sup>/mol), respectively, at 77 K (Figure S4). Fitting these data to the Barrett–Joyner–Halenda (BJH) pore size distribution model<sup>18</sup> with the Kruk–Jaroniec–Sayari correction for hexagonal pores<sup>19</sup> provided pore sizes of 20.5 and 20.3 Å for **2** and **3**, respectively (Figure S7). These are smaller than the pore size of **1** (22.9 Å) and are in agreement with pore narrowing due to protrusion of the terminal halides into the pores of the oxidized MOFs and the decreased unit cell parameters stemming from the smaller ionic radius of Co(III).

The robustness demonstrated by **1** in the presence of elemental Cl<sub>2</sub> and Br<sub>2</sub> is remarkable. Previous attempts to capture elemental Cl<sub>2</sub> in a MOF led to nearly complete loss of crystallinity of the parent materials.<sup>20</sup> We attribute the stability of **2** and **3** in part to the quantitative formation of kinetically inert low-spin Co(III) centers. Notably, MOFs made exclusively from Co(III) SBUs are themselves unprecedented. Indeed, the only previous examples of MOFs containing Co(III) in the nodes are cases of mixed-valent Co(II)/Co(III) materials<sup>21–23</sup> or examples where the presence of dilute Co(III) within a native Co(II) MOF has been inferred from its catalytic activity.<sup>24,25</sup>

**Thermal Release of Elemental Halogens from Oxidized MOFs.** Thermogravimetric analysis (TGA) of dry samples of **2** and **3** under a stream of He revealed surprisingly sharp weight loss steps at approximately 275 and 195 °C, respectively, and no subsequent weight losses up to approximately 450 °C (Figure 3). Compound **1** itself did not exhibit any weight loss up to 400 °C. These data suggested that **2** and **3** may eliminate elemental halogens thermally. Coupling

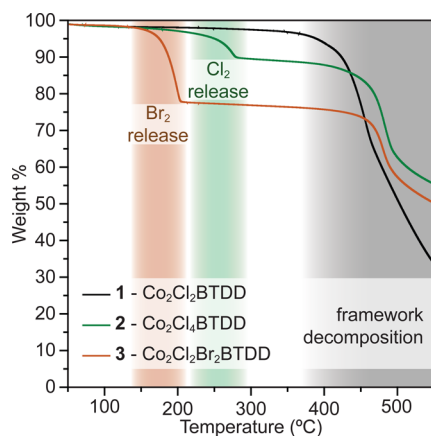


**Figure 3.** Thermogravimetric analyses. The TGA plot of **1** (black line) shows that framework decomposition occurs at ca. 400 °C. Abrupt weight losses corresponding to halogen liberation from **2** (green line) and **3** (brown line) are emphasized in the green and brown regions, respectively.

the thermogravimetric analyzer with an in-line mass spectrometer confirmed this hypothesis. The ion flux, which peaked at temperatures coinciding with those promoting weight loss observed by TGA, primarily consisted of  $X_2^+$  ions and ionized halogen decomposition products (further details are provided in the [Supporting Information](#)). For **2** the primary species were  $^{35}\text{Cl}^+$  and  $^{37}\text{Cl}^+$  as well as the corresponding hydrogen chloride isotopologues ([Figure S10](#)). Importantly, we also detected the masses of the two major isotopologues of  $\text{Cl}_2$ :  $^{70}\text{Cl}_2^+$  (57.4% natural abundance) and  $^{72}\text{Cl}_2^+$  (36.3% abundance). For **3**, we observed all three isotopologues of molecular bromine, namely,  $^{158}\text{Br}_2^+$ ,  $^{160}\text{Br}_2^+$ , and  $^{162}\text{Br}_2^+$ , with their expected natural abundances (25.7%, 50.0%, and 24.3%, respectively), as well as their decomposition products, including ionized bromine atoms and hydrogen bromide ions ([Figure S11](#)).

Thermal elimination of  $X_2$  from both **2** and **3** occurs without notable losses of crystallinity or porosity. PXRD analysis of **2** and **3** after halogen elimination by thermal treatment at 300 and 210 °C, respectively, revealed patterns that were identical to that of **1**, the all-Co(II) parent material ([Figure S2](#)).  $\text{N}_2$  adsorption isotherms of thermally treated samples of **2** and **3** showed total uptakes of 550 and 660  $\text{cm}^3/\text{g}$ , respectively ([Figure S5](#)). Both isotherms can be fitted to reveal very narrow pore size distributions peaking at 22.6 Å, again very close to the original value of 22.9 Å found in **1** ([Figure S7](#)). Together, the TGA and gas sorption data suggest that the majority of Co(III) sites in **2** and **3** are reduced to Co(II) upon thermal halogen elimination.

Further confirmation of the reversible uptake/release of halogens by **1** came from *in situ* XAS studies of  $\text{Cl}_2$  elimination. Thus, following the position of the Co K-edge energy while heating **2** from room temperature to 290 °C revealed essentially no change below 200 °C and a progressive decrease between 200 and 290 °C. Additionally, the pre-edge absorption peak intensity at ca. 7709 eV increases upon heating, indicating a gradual conversion of the Co coordination geometry from octahedral to square-pyramidal ([Figure 2A](#)). Linear combination analysis performed on the whole series of XANES spectra using the spectra of **1** and **2** at room temperature as references allowed us to quantify the transformation of **2** to **1** ([Figures 2D](#) and [S17](#)). The content of **2** decreased steadily from 91% at 207 °C to less than 2% at 285 °C, where the position and shape of

the XANES spectrum nearly coincided with those of **1** ([Figure 2A](#)). The higher residual signal and increased R-factor values observed at the highest temperature points suggest that the product obtained by thermal treatment of **2** is very similar to **1** but exhibits a higher degree of static structural disorder relative to the latter. An equivalent trend is observed in the EXAFS spectra. The weakening of the EXAFS signal stemming from the Cl-shell scattering ([Figure 2B](#)) and the progressive elongation of the first-shell bond distances, evident from the imaginary component ([Figure 2C](#)), are consistent with reduction of the majority of the MOF nodes from Co(III) to Co(II).

Although the *in situ* XANES data suggest that the conversion from **2** to **1** is nearly complete at the end of the thermal treatment ([Figure 2D](#), left ordinate axis), the weight losses observed under the milder TGA conditions (9.5 and 21 wt % for **2** and **3**, respectively) correspond to elimination of only 70–80% of the theoretical halogen content. Thermal treatment of bulk samples of **2** and **3** under vacuum gave products with elemental formulas of  $\text{Co}_2\text{Cl}_{2.4}\text{BTDD}$  and  $\text{Co}_2\text{Cl}_2\text{Br}_{0.34}\text{BTDD}$ , respectively, which also indicate loss of only approximately 80% of the releasable halogen content. Iodometric titration of  $\text{Br}_2$  trapped from thermal treatment of **3** confirmed that the isolated yield of  $\text{Br}_2$  under these conditions is close to 80% ([Table S2](#)). Importantly, the loss of  $\text{Br}_2$  determined by iodometry never exceeded that observed by TGA, confirming that the species eliminated from **3** is indeed  $\text{Br}_2$  and not lighter halogens such as  $\text{Cl}_2$  or  $\text{BrCl}$ , as might be expected if the original bridging chlorides were involved in the elimination. The apparent quantitative discrepancy between the TGA and XANES data stems from the average character of the XAS technique, which complicates the assignment of a minor fraction of unreacted Co(III) sites. Indeed, the spectrum of **2** collected after heating (spectrum 14; [Figure 2D](#), right ordinate axis) has an R factor that is more than 3 times larger than those of the preceding sequential spectra collected during heating. The higher level of static disorder evidenced by EXAFS analysis of **2** after heating matches well with the possible presence of 10–20% of Co(III) sites that coordinate three Cl atoms in the first shell in a slightly distorted environment (also see section 9.3 in the [Supporting Information](#)).

Importantly, **1** can store and release halogens more than once: three consecutive cycles of exposure of **1** to  $\text{Br}_2$  vapors and thermal  $\text{Br}_2$  release gave a reproducible recovery of 75–80% of the theoretical  $\text{Br}_2$  yield with retention of structural integrity and crystallinity and only minimal deterioration of porosity, as confirmed by SEM, PXRD, and  $\text{N}_2$  adsorption measurements after each cycle ([Figures S18](#), [S3](#), and [S6](#), respectively). Altogether, these data suggest that a recovery yield of 80% is what should be expected in practice when using **1** for the reversible storage of halogens for the first cycle, with the yield becoming essentially quantitative on subsequent cycles.

**Mechanistic Considerations of  $X_2$  Release.** The persistent 80% recoverable yield of halogens under cycling conditions is intriguing. It implies that there may be an inherent preference, thermodynamic or kinetic, for approximately 20% of the Co atoms in **2** and **3** to remain oxidized. To advance a hypothesis for this unexpected behavior, one may examine plausible  $X_2$  elimination mechanisms from **2** or **3**. Considering only terminal halogen elimination pathways, as the bridging halogens are structurally integral, possible  $X_2$  formation routes include recombination of two  $X^\bullet$  radicals, attack of  $X^\bullet$  onto a

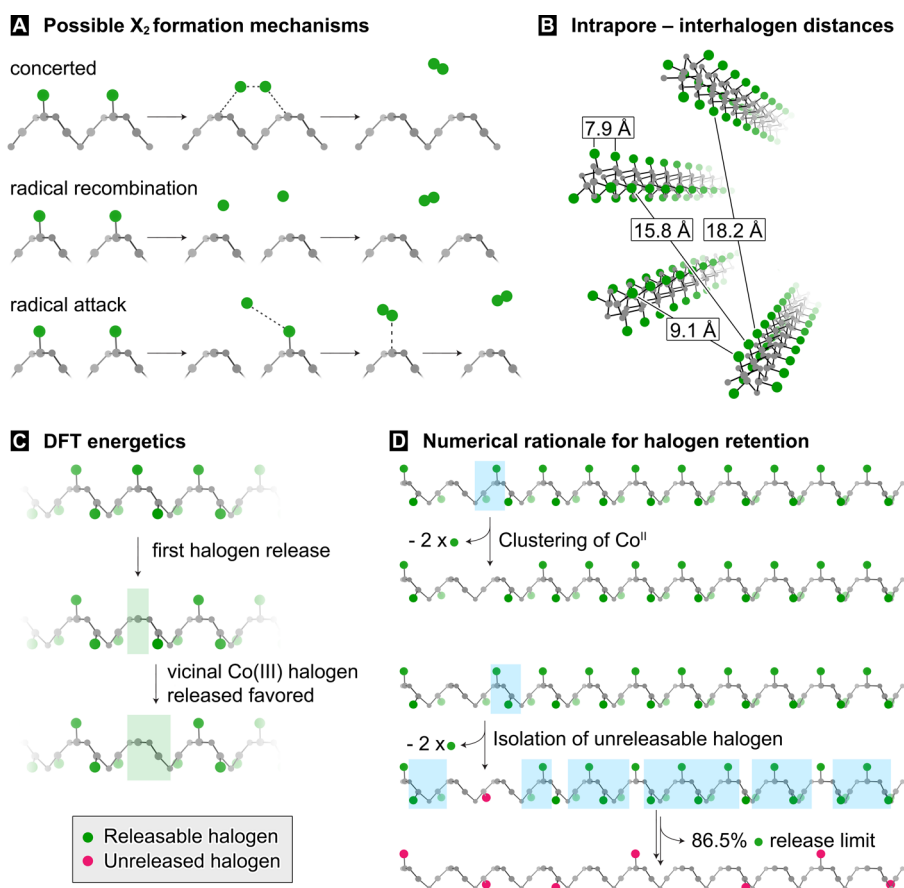


**Figure 4.**  $X_2$  formation rationale. (A) Three possible mechanisms for the formation of elemental halogens. The concerted mechanism can be thought to have formal radical character, while both the recombination and attack schemes feature transient  $X^\bullet$  species. (B) The nearest intrapore halogen neighbors are separated by 7.9 Å. (C) DFT calculations predict that vicinal removal of halogens is most favored. (D) Graphical representation of our probabilistic model for halogen removal depicting the route to the retention of 13.5% terminal halogens.

terminal halide species, or the concerted formation of  $X_2$  without the intermediacy of  $X^\bullet$  (Figure 4A). Although the shortest distance between terminal halides is 6.5 and 6.8 Å for 2 and 3, respectively, concerted  $X_2$  elimination from these nearest intrachain neighbors is physically impossible because the two X atoms point into neighboring pores, such that concerted formation of an X–X bond is obstructed by a structurally integral bridging Cl atom. There are several alternative pairs of terminal halide atoms that would allow elimination of  $X_2$  (i.e., elimination would occur from within the same pore). However, the shortest X...X distance for these intrapore elimination routes is 7.8 and 7.9 Å for 2 and 3, respectively, which is too long for a concerted  $X_2$  elimination mechanism (Figure 4B). Therefore, elimination of  $X_2$  *must* occur through a radical mechanism via homolytic cleavage of the terminal Co(III)–X bonds. What, then, prevents the complete conversion of all Co(III)–X species to Co(II) and quantitative formation of  $X_2$ ?

To probe the thermodynamics of halogen release, we employed density functional theory (DFT) calculations on a  $1 \times 1 \times 2$  expansion of the crystallographic unit cell, which yielded six unique Co centers per periodic chain. By sampling all of the possible elimination combinations, we found that generating pairs of immediately adjacent Co(II) centers occurs with no further energetic penalty relative to generating the first Co(II) center. In other words, elimination of an X atom from a Co(III)–X moiety immediately adjacent to an existing Co(II) center is thermodynamically favored relative to the formation of

another isolated Co(II) center (Figure S23). The DFT model makes no inference regarding the fate of the departing halogen atoms but rather considers the energetics of the residual dehalogenated Co chains. These computations therefore suggest that halogen release is pairwise through the mechanism shown schematically in Figure 4C. Further removal of halogens from our truncated model posed computational challenges (the limitations are discussed in detail in the Supporting Information).

Combining the DFT result of nearest-neighbor elimination and our experimental observation of formation of  $X_2$ , we can construct a probabilistic model in which random pairs of Co(II) centers are formed from an infinite chain of Co(III) centers, as shown in Figure 4D. With the only initial criterion being pairwise vicinal removal of halogens, this model predicts a residual Co(III)–X content of 13.5%, corresponding to halogen release of 86.5% of the theoretical maximum (the complete mathematical derivation is presented in the Supporting Information). This is in remarkably good agreement with our experimental data given the simplicity of our mathematical model and the size limitations of our computational model. Combining these models, we conclude that our experimental retention of approximately 20% of the terminal Co-bound halogens is exemplary of the high performance of **1** for reversible halogen capture and release.

## CONCLUSION

Uptake of elemental halogens, Cl<sub>2</sub> and Br<sub>2</sub>, by a robust Co(II) azolate MOF occurs without loss of crystallinity or porosity. Subsequent thermal treatment of the oxidized materials releases the elemental halogens, closing a cycle that amounts to reversible capture and release of these highly corrosive gases. This cycling behavior is unprecedented in MOFs, which are typically decomposed by or react irreversibly with the lighter halogens. The unusual reactivity here is enabled by the quantitative formation of Co(III) SBUs, also unique for MOFs, and the facile homolytic cleavage of Co(III)–X bonds<sup>26</sup> to form X<sub>2</sub> through a radical mechanism. These results provide a blueprint for the design of other porous materials geared toward the capture and storage of noxious, corrosive gases through reversible chemisorptive mechanisms.

## ASSOCIATED CONTENT

### Supporting Information

The Supporting Information is available free of charge on the ACS Publications website at DOI: 10.1021/jacs.7b02161.

Experimental procedures; structural data on **1**, detailed characterization of **2** and **3**, including NPD and PXRD patterns, N<sub>2</sub> adsorption isotherms, TGA data, magnetic measurements, XAS data, and SEM images; and comprehensive computational methods (PDF)

## AUTHOR INFORMATION

### Corresponding Author

\*mdinca@mit.edu

### ORCID

Christopher H. Hendon: 0000-0002-7132-768X

Carlo Lamberti: 0000-0001-8004-2312

Mircea Dincă: 0000-0002-1262-1264

### Notes

The authors declare no competing financial interest.

## ACKNOWLEDGMENTS

Studies of metal–small-molecule interactions in the Dincă lab are supported by a CAREER Award to M.D. from the National Science Foundation (DMR-1452612). M.D. acknowledges the Sloan Foundation, the Research Corporation for Science Advancement (Cottrell Award), and 3M for nontenured faculty funds. Y.T. gratefully acknowledges the MIT–Technion Postdoctoral Fellowship Program. A.W.S. gratefully acknowledges the National Science Foundation Graduate Research Fellowship program for financial support under Grant No. 1122374. J.D.T. gratefully acknowledges research support from the US DOE Office of Energy Efficiency and Renewable Energy, Fuel Cell Technologies Office, under Contract no. DE-AC36-08GO28308. We thank Dr. G. Agostini for assistance with the XAS data collection at ESRF BM23 and Dr. H. Müller for his support in the ESRF chemistry lab. C.L. and K.A.L. acknowledge the Mega-grant of the Russian Federation Government (14.Y26.31.0001). We thank Mr. W. F. DiNatale at the Institute of Soldier Nanotechnology (ISN) for assistance with SEM and Dr. C. Settens at the MIT Center for Materials Science and Engineering (CMSE) for assistance with capillary PXRD measurements. This work used the Extreme Science and Engineering Discovery Environment (XSEDE), which is supported by National Science Foundation grant number ACI-1548562.

## REFERENCES

- (1) Fauvarque, J. *Pure Appl. Chem.* **1996**, *68*, 1713.
- (2) McDonald, R. B.; Merriman, W. R. *Special Publication, Chem. Soc.* **1977**, *31*, 168.
- (3) Murray, L. J.; Dincă, M.; Yano, J.; Chavan, S.; Bordiga, S.; Brown, C. M.; Long, J. R. *J. Am. Chem. Soc.* **2010**, *132*, 7856.
- (4) Xiao, D. J.; Gonzalez, M. I.; Darago, L. E.; Vogiatzis, K. D.; Haldoupis, E.; Gagliardi, L.; Long, J. R. *J. Am. Chem. Soc.* **2016**, *138*, 7161.
- (5) Bloch, E. D.; Queen, W. L.; Chavan, S.; Wheatley, P. S.; Zadrozny, J. M.; Morris, R.; Brown, C. M.; Lamberti, C.; Bordiga, S.; Long, J. R. *J. Am. Chem. Soc.* **2015**, *137*, 3466.
- (6) Yang, S.; Sun, J.; Ramirez-Cuesta, A. J.; Callear, S. K.; David, W. I. F.; Anderson, D. P.; Newby, R.; Blake, A. J.; Parker, J. E.; Tang, C. C.; Schröder, M. *Nat. Chem.* **2012**, *4*, 887.
- (7) Britt, D.; Tranchemontagne, D.; Yaghi, O. M. *Proc. Natl. Acad. Sci. U. S. A.* **2008**, *105*, 11623.
- (8) Morris, W.; Doonan, C. J.; Yaghi, O. M. *Inorg. Chem.* **2011**, *50*, 6853.
- (9) Katz, M. J.; Howarth, A. J.; Moghadam, P. Z.; DeCoste, J. B.; Snurr, R. Q.; Hupp, J. T.; Farha, O. K. *Dalton Trans.* **2016**, *45*, 4150.
- (10) Rieth, A. J.; Tulchinsky, Y.; Dincă, M. *J. Am. Chem. Soc.* **2016**, *138*, 9401.
- (11) Marshall, R. J.; Griffin, S. L.; Wilson, C.; Forgan, R. S. *Chem. - Eur. J.* **2016**, *22*, 4870.
- (12) Brozek, C. K.; Dincă, M. *J. Am. Chem. Soc.* **2013**, *135*, 12886.
- (13) Xiao, D. J.; Bloch, E. D.; Mason, J. A.; Queen, W. L.; Hudson, M. R.; Planas, N.; Borycz, J.; Dzubak, A. L.; Verma, P.; Lee, K.; Bonino, F.; Crocellà, V.; Yano, J.; Bordiga, S.; Truhlar, D. G.; Gagliardi, L.; Brown, C. M.; Long, J. R. *Nat. Chem.* **2014**, *6*, 590.
- (14) Moen, A.; Nicholson, D. G.; Running, M.; Lamble, G. M.; Lee, J.; Emerich, H. J. *Chem. Soc., Faraday Trans.* **1997**, *93*, 4071.
- (15) Rossin, A.; Di Credico, B.; Giambastiani, G.; Peruzzini, M.; Pescitelli, G.; Reginato, G.; Borfecchia, E.; Gianolio, D.; Lamberti, C.; Bordiga, S. *J. Mater. Chem.* **2012**, *22*, 10335.
- (16) Cozzolino, A. F.; Brozek, C. K.; Palmer, R. D.; Yano, J.; Li, M.; Dincă, M. *J. Am. Chem. Soc.* **2014**, *136*, 3334.
- (17) Dietzel, P. D. C.; Morita, Y.; Blom, R.; Fjellvag, H. *Angew. Chem., Int. Ed.* **2005**, *44*, 6354.
- (18) Barrett, E. P.; Joyner, L. G.; Halenda, P. P. *J. Am. Chem. Soc.* **1951**, *73*, 373.
- (19) Kruk, M.; Jaroniec, M.; Sayari, A. *Langmuir* **1997**, *13*, 6267.
- (20) DeCoste, J. B.; Browe, M. A.; Wagner, G. W.; Rossin, J. A.; Peterson, G. W. *Chem. Commun.* **2015**, *51*, 12474.
- (21) Zhang, S.; Liu, X.; Liu, L.; Xia, Z.; Wang, W.; Yang, Q.; Ke, H.; Wei, Q.; Xie, G.; Chen, S.; Gao, S. *Sci. China: Chem.* **2015**, *58*, 1032.
- (22) Wei, Y.; Chen, K.; Liao, P.; Zhu, B.; Lin, R.; Zhou, H.; Wang, B.; Xue, W.; Zhang, J.; Chen, X. *Chem. Sci.* **2013**, *4*, 1539.
- (23) Liao, P.-Q.; Chen, H.; Zhou, D.-D.; Liu, S.-Y.; He, C.-T.; Rui, Z.; Ji, H.; Zhang, J.-P.; Chen, X.-M. *Energy Environ. Sci.* **2015**, *8*, 1011.
- (24) Tonigold, M.; Lu, Y.; Bredenkötter, B.; Rieger, B.; Bahnmüller, S.; Hitzbleck, J.; Langstein, G.; Volkmer, D. *Angew. Chem., Int. Ed.* **2009**, *48*, 7546.
- (25) Lu, X.; Liao, P.; Wang, J.; Wu, J.; Chen, X.; He, C.; Zhang, J.; Li, G.; Chen, X. *J. Am. Chem. Soc.* **2016**, *138*, 8336.
- (26) Schrauzer, G. N.; Sibert, J. W.; Windgassen, R. J. *J. Am. Chem. Soc.* **1968**, *90*, 6681.